RSC Advances

PAPER

View Article Online
View Journal | View Issue

Cite this: *RSC Adv.*, 2025, **15**, 9952

PDMS biointerfaces featuring honeycomb-like well microtextures designed for a pro-healing environment

Andreea Mariana Negrescu, †[ab] Simona Nistorescu,†[ac] Anca Bonciu, [c] Laurentiu Rusen, [c] Nicoleta Dumitrescu,[c] Iuliana Urzica,[c] Antoniu Moldovan,[c] Patrick Hoffmann,[d] Gratiela Gradisteanu Pircalaboiu,[ae] Anisoara Cimpean *[a] and Valentina Dinca *[c]

Even today, the reduction of complications following breast implant surgery together with the enhancement of implant integration and performance through the modulation of the foreign body response (FBR), remains a fundamental challenge in the field of plastic surgery. Therefore, tailoring the material's physical characteristics to modulate FBR can represent an effective approach in implantology. While polydimethylsiloxane (PDMS) patterning on 2D substrates is a relatively established and available procedure, micropatterning multiscaled biointerfaces on a controlled large area has been more challenging. Therefore, in the present work, a specific designed honeycomb-like well biointerface was designed and obtained by replication in PDMS at large scale and its effectiveness towards creating a pro-healing environment was investigated. The grayscale masks assisted laser-based 3D texturing method was used for creating the required moulds in Polycarbonate for large area replication. By comparison to the smooth substrate, the honeycomb topography altered the fibroblasts' behaviour in terms of adhesion and morphology and reduced the macrophages' inflammatory response. Additionally, the microstructured surface effectively inhibited macrophage fusion, significantly limiting the colonization of both Gram-positive and Gram-negative microbial strains on the tested surfaces. Overall, this study introduces an innovative approach to mitigate the *in vitro* FBR to silicone, achieved through the creation of a honeycomb-inspired topography for prosthetic interfaces.

Received 3rd January 2025
Accepted 21st March 2025

DOI: 10.1039/d5ra00063g

rsc.li/rsc-advances

Introduction

Since their first introduction in the 60s, breast implants have been used with the purpose of modifying or replacing an individual's mammary tissue, either for cosmetic (breast augmentation) or reconstructive indications, where the prosthesis is utilised to remodel a deformed or absent breast following a mastectomy.[1–5]

Textured breast implants were used in over 35 million cases according to a survey conducted in 2020.[3] Since breast reconstruction after mastectomy will have a significant impact on the long-term body image, quality of life, and mental health of the afflicted women, it is important for clinicians to be in touch with the most advanced trends in breast reconstructive surgery.[6,7] Therefore, in the last decades, implant-based breast reconstruction has surpassed autologous techniques despite the obvious long-term superiority of the latter. This clear shift of direction was mainly attributed to the faster recovery period, the simplicity of the technique, and the absence of the morbidity at the donor-site, but at the price of a less impressive aesthetic outcome.[8,9] The main issues to be tackled in the case of breast implants, besides silicone leakage in silicone-filled implants and implant malposition, are related to the effect of the given interface and its characteristics onto the surrounding tissues (*e.g.* infection, capsular contracture).[10–16] Therefore, the use of silicone elastomer polydimethylsiloxane (PDMS),[17] provides an optimal combination of flexibility, strength, biocompatibility, ease of manufacture and low production costs, rendering it well-suited for breast implant shell fabrication. For example, one of the most frequently occurring complications which accompanies the implantation of a silicone-based medical device is represented by the formation of a capsular contracture, a phenomenon experienced by up to 50% of females subjected

[a]*Faculty of Biology, University of Bucharest, Splaiul Independenței 91-95, 050095 Bucharest, Romania. E-mail: anisoara.cimpean@bio.unibuc.ro*

[b]*Research Institute of the University of Bucharest (ICUB), University of Bucharest, 050657 Bucharest, Romania*

[c]*National Institute for Lasers, Plasma, and Radiation Physics, 409 Atomistilor Street, 077125, Romania. E-mail: valentina.dinca@inflpr.ro*

[d]*Laboratory for Advanced Materials Processing, EMPA, Swiss Federal Institute for Materials Science and Technology, Feuerstrasse 39, CH-3602 Thun, Swizerland*

[e]*Polytechnic University of Bucharest, Splaiul Independenței 313, Bucharest, 060042, Romania*

† Andreea M. Negrescu and Simona Nistorescu contributed equally.

to mammaplasty.[18] Clinically significant, the capsular contracture, is characterized by an overaccumulation of fibrotic tissue that surrounds the implant shell and leads to firmness, deformity, pain and finally device failure.[19] Moreover, in severe cases an additional surgery is required, but more than often these interventions are unpredictable, and they do not guarantee a successful result without recurrence.[20] Even to this date, the exact mechanism underlying the capsular contracture remains a mystery, but from what is known, it is very clear that the host's immune system has an essential role in its development. In addition, it was found that peri-prosthetic infections and radiation therapy before and after implant introduction, can pose as risk factors, while insertions under the pectoralis major muscle and in particular textured surfaces instead of smooth ones, can minimise the excessive fibrotic capsule formation.[21] In the last decades, numerous advances in both material characteristics and, especially, in interface design, have provided feasible strategies for mitigating this immune-mediated reaction.[22] Thus, these approaches which envisage changes in the physical parameters of the biomedical implant (*e.g.*, chemical and physical properties), can influence the biomaterial's integration process and, ultimately, dictate its *in vivo* fate. For example, the chemical modification of an implant's surface through a fine-cell polyurethane coating, despite its positive effect on tissue ingrowth enhancement due to its open-pore texture,[23] was shown to give rise to toxic hydrolysis products upon its *in vivo* degradation.[24] Therefore, one straightforward, promising strategy that can avoid material degradation is represented by interface texturing, a technique that provides a specifically designed surface with distinct microenvironment characteristics that can influence the bio-integration process. Surface texturing is usually achieved by altering the biomaterial's topography and includes techniques such as imprinting, replication, salt-loss, and the gas expansion method which leads to the so-called nanotextured (80–100 μm^2), microtextured (100–200 μm^2) or macrotextured (200–300 μm^2) implants.[25] Moreover, recently the textured interfaces were classified as "peaks and valleys," "open cavities," and "semi-opened cavities"[26] so for example, the majority of the commercially available implants, which are characterized by rougher surfaces, presents either cuboid-shaped pits or nodular characteristics.[27] Nevertheless, despite the numerous studies reporting the positive impact of texturing on the incidence of both implant malposition and the formation of the capsular contracture, a correlation between the modified interfaces with a pore size larger than 300 μm and the evolution of breast implant-associated anaplastic large cell lymphoma (BIA-ALCL)[28] has been observed, mainly due to their ability to elicit an excessive inflammation and a chronic antigenic stimulation due to the bacteria-associated infection.[29–31]

A substantial body of evidence from recent decades, including our own research,[32–35] underscores the significant influence of a controlled nano- and micro-topography on the cellular behaviour, evidencing that, when microscale topographies were employed, a guidance in the cell's shape, motility and adhesion was observed, whereas nanoscale features have been shown to regulate the anchorage-dependent cells by targeting the integrin receptors found in the focal adhesions, thereby modulating the intracellular signalling and behaviour (*i.e.* from bactericidal effects of nanopillars and nanospikes to 65% cellular adhesion reduction for human dermal fibroblasts' adhesion up for hexagonal and square patterns pits with 5 μm diameter in silicone and nanocellulose).[35–38] However, with regard to the elastomeric surfaces employed in implants as well as in research studies, it was demonstrated that various surface topographies, differing in material feature sizes, microstructure organization (*e.g.*, ordered or random), and porosity, can affect cellular behaviour from bacteria adhesion to macrophage polarization. These studies highlight the importance of tailoring surface topographies to specific size scales and geometries to effectively mitigate FBR in case of? PDMS-based implants. For example, Chen *et al.*[39] observed that 2 μm gratings significantly reduced macrophage density and *in vivo* cell fusion. Similarly, Doloff *et al.* (2021)[40] demonstrated that amongst different silicone elastomer (PDMS) implants with varying micro-textures (R: 0–90 μm), the surface with a roughness of 4 μm was capable of suppressing FBR and fibrosis in both a mouse and rabbit model. However, the immunomodulatory effects of topography are complex, and specific design rules for topographical features that promote distinct macrophage phenotypes are not yet established.

Xu *et al.*[41] explored the effects of specific topographical dimensions on macrophage-mediated bacterial phagocytosis. Their co-culture studies with *E. coli* on patterned recessive PDMS wells identified a critical threshold dimension that impaired phagocytosis: square wells with a side length of 5 μm and depth of 10 μm reduced phagocytosis by up to 100-fold compared to flat surfaces or larger patterns (>10 μm). This reduction was attributed to physical limitations on macrophage pseudopodia extension and bacterial accessibility. Additionally, increasing the spacing between wells (*e.g.*, 50 μm) exacerbated the impairment, further reducing macrophage activity.

Within this scale range, a recent study[32] showed that by designing surfaces with multiscaled interrupted geometries based on microlines units, the bacterial colonization and macrophage activation towards a pro-inflammatory profile were mitigated through the mechanical interdigitation within the multiscaled surface morphology, independent of the surface chemical properties. The proposed topographies obtained by PDMS replica using moulds obtained by photolithography considered using rectangular step-like feature and a 250 nm step size, with multiscaled in depth distribution as well spacing varying from 900 nm to tens of microns targeting to understand how mixed textures might offer superior resistance towards bacterial colonisation while fostering an anti-inflammatory microenvironment.

Moreover, by modifying the silicone surface, for instance, through the replication of the acellular dermal matrix (ADM) or the introduction of roughness of around 4 μm, a notable influence on the capsule's structure and morphology can be exerted. Thus, by increasing the complexity of the surface's topography a distinct alteration in the pathophysiology of the FBR could be obtained, ultimately yielding a diminished inflammatory response in contrast to the more prevalent commercially available silicone implant surfaces.[40,42–45]

Therefore, taking in consideration that the optimal lateral feature sizes for an effective reduction of FBR, cell proliferation enhancement, promotion of extracellular matrix (ECM) production and immune modulation regulation, were shown to be in the range of 20–50 μm, the present study proposes new honeycomb-like wells of microtextured PDMS-based shell interfaces obtained by replication using moulds obtained by a process of laser texturing assisted by a grayscale mask. In this regard, microscale features of hexagonal matrices with lateral dimensions of 51 μm (±500 nm) unit, 5 μm depth, 25 μm internal length per unit, base width of walls of 17 μm and top width of ridge of 8 μm, were accurately and reproducibly replicated in PDMS. While topographies such as grooves, pillars, regular, irregular have their own advantages, the proposed honeycomb structures address multiple aspects of FBR simultaneously by providing geometric control of microstructures at specific scales by the unique system involving grey level masks assisted laser texturing for moulds production on large areas; and a disruption in the fibroblasts' adhesion and a reduction in the macrophages' activation.

Since fibrotic tissue encapsulation of the silicone-based implant represents one of the most common causes for device failure, the fibroblast activation-suppressing features of the newly developed microtextured surface was investigated in comparison to the smooth PDMS using the CCD-1070Sk fibroblasts. Additionally, due to the macrophages' involvement in the FBR evolution through their regulatory role in inflammation and wound healing (*via* their tunable polarization state and the recruitment of fibroblasts through cytokine secretion), the behaviour of the RAW 264.7 macrophages was also investigated. Furthermore, given that the bacterial infection is implicated in the fibrotic response to the implantable biomaterials and the evolution of BIA-ALCL, the hindering effect of PDMS structuring on biofilm formation was assessed against three standard strains, namely *Staphylococcus aureus* (*S. aureus*), *Escherichia coli* (*E. coli*), and *Candida albicans* (*C. albicans*).

Despite the fact that PDMS (Sylgard 184) is designed mainly for research applications, and it lacks the medical-grade certification, our approach was to be used as a model for research purpose to support the method for obtaining reproducible patterns on large areas that can be also easily extended to the structuring of silicone elastomers.

Altogether, this unique study aims at demonstrating that the macrophages and fibroblasts' response to silicone topographies can be tailored to induce physiological changes in cells, thus paving the way for further research focused on developing biomaterials capable of eliminating the capsular contracture by subverting FBR.

Experimental details

Moulds and substrates production

A system comprising grey level mask and a KrF excimer laser (Exitech PPM-601E Gen6 Tool, Oxford, UK), (248 nm wavelength, 50 Hz repetition rate, 20 ns pulse) was used to structure hexagonal pillars in polycarbonates (PC) sheets following a procedure as outlined in.[45] In order to create a larger area, the mask was moved in a controlled manner under the beam and the matrices of the hexagonally shaped pillars were obtained in PC by direct laser ablation using 20 pulses, with average fluence of 400 mJ per cm^2 per pulse. The PC ablation residue particles due to laser ablation were aspired during the texturing process. All the surfaces were cleaned by ultrasonication for 10 minutes, sequentially, in ethanol and double distilled water. Once dried, the moulds were placed in Petri dishes and a mixture of 10 : 1 weight ratio of Dow Sylgard 184 base and curing agent was poured on top of it. In order to remove the air bubbles produced during the chemical reaction of the base and curing agent, the mixture was maintained for 20 minutes at room temperature, poured on the PC master, and cured at room temperature. After 48 h, the replicated PDMS samples were removed from the mould, immersed in ethanol for 10 minutes, respectively in double distilled water (until before use). The drying of the samples was performed with argon gas. Once cleaned, all the samples were subjected to 2 h treatment using UV ozone lamp, and maintained in sterile water until they were to be used for biological assays.

Substrates characterization

Scanning electron microscopy (SEM), as well as atomic force microscopy (*i.e.*, AFM), were used for analysing the morphological features of the PDMS substrates. JSM-531 Inspect S Electron Scanning Microscope (accelerating voltages: 5 to 25 kV) was used for the top view topographical investigations. Detailed profile of the structures walls was obtained in non-contact mode by AFM investigations (XE100 AFM, Park Systems), in ambient conditions. Adhesion measurements employing silicon tips with a resonance frequency of ∼70 kHz and an elastic constant of 2 N m^{-1} were evaluated through force–distance analysis at three randomly selected points of varying heights.

Surface topography parameters such as the arithmetical mean height (Sa, μm), root mean square height (Sq, μm), peak-to-valley height (Sz, μm), maximum valley depth (Sv), maximum peak height (Sp), skewness (Ssk), and kurtosis (Sku), were measured using the XP-2 Stylus-Profiler System (vertical resolution of 1.5 Å, applied force of 2 mg, scanning rate 0.01 mm s^{-1}). Data analysis for surface roughness was performed with the TrueMap v4 software package by Ambios Technology. The results are reported as the mean ± standard deviation based on 60 measurements, covering at least six randomly chosen 140 × 140 μm^2 areas on each substrate surface.

Contact angle and surface free energy measurements

Prior to the experiments, the clean PDMS samples were exposed for 2 h to an ultraviolet (UV) ozone lamp. To assess the wettability characteristics of both smooth and textured PDMS samples, we conducted contact angle measurements using the sessile drop method with a KSV CAM101 microscope from KSV Instruments Ltd (Espoo, Finland), all conducted at a constant room temperature of 20 °C. Surface free energy (SFE) was determined, using the Owens, Wendt, Rabel, and Kaelble (OWRK) method, with two wetting agents, namely water and di-

iodomethane.[46] At least six independent measurements were taken from various areas of each sample.

Investigation of the *in vitro* cell behaviour

Cell culture. In the present study, the experiments were performed on two different cell lines, namely the CCD-1070Sk human fibroblasts and the murine RAW 264.7 macrophages. Both cell lines were purchased from American Type Culture Collection (ATCC, Manassas, VA, USA) and grown in Dulbecco's Modified Eagle Medium (DMEM, Sigma-Aldrich Co., St. Louis, MO, USA) supplemented with 10% (v/v) fetal bovine serum (FBS, Life Technologies Corporation, Grand Island, NY, USA) and 1% (v/v) penicillin (10 000 units per mL)/streptomycin (10 mg mL^{-1}) (Sigma-Aldrich Co., St. Louis, MO, USA) in a humidified atmosphere of 5% CO_2 at 37 °C. For the experiments, the fibroblasts were seeded in triplicates directly onto the surface of the sterile PDMS supports at an initial density of 10^4 cells per cm^2 and maintained for various time periods in standard culture conditions depending on the analysed cellular parameter. Likewise, the cellular response of the adherent RAW 264.7 macrophages was also investigated. Therefore, the investigation of cell viability, proliferation and morphology required an initial cell density of 10^4 cells per cm^2, while the inflammatory mediators' quantification and macrophage fusion assay necessitated an initial cell density of 8×10^4 cells per cm^2 and 5×10^3 cells per cm^2, respectively. It is noteworthy, that the inflammatory activity analysis was performed under standard and pro-inflammatory conditions (treatment with 100 ng per mL *E. coli* lipopolysaccharide (LPS, Sigma-Aldrich Co., St. Louis, MO, USA)). For each type of sample, all cell-culture based assays have been conducted in triplicate sets.

In vitro cell survival and proliferation assessment

To differentiate the living cells from the dead ones, after 1- and 3-days in culture, a live/dead viability/cytotoxicity kit (Molecular Probes, Eugen, OR, USA) was employed, as previously reported.[47] The stained cells were observed with an inverted fluorescent microscope (Olympus IX71, Olympus, Tokyo, Japan) and the representative images were acquired with the cellSense Dimension acquisition system Version 4.1. Furthermore, at the same incubation periods, a Cell Counting Kit-8 (CCK-8, Sigma-Aldrich Co., St. Louis, MO, USA) was used in accordance to the manufacturer's instructions,[48] to determine the potential of the two PDMS surfaces to sustain cell proliferation.

Cell morphology assessment

In order to observe the degree of cell spreading and their distinct morphological characteristics, the fluorescent staining of the actin cytoskeleton with phalloidin conjugated with AlexaFlour 488 was performed as described previously.[49] In addition, the immunofluorescence assay was also used to reveal the vimentin intermediate filaments expressed by the CCD-1070Sk cells. Following fixation, permeabilization and blocking, the cellular monolayer was firstly stained with an anti-vimentin primary antibody (Santa Cruz Biotechnology, dilution 1 : 50) for 2 h, and subsequently incubated for 1 h, in the dark, with an anti-mouse secondary antibody labelled with fluorescein isothiocyanate (FITC) (Santa Cruz Biotechnology, dilution 1 : 200). An inverted fluorescence microscope (Olympus IX71, Olympus, Tokyo, Japan) was used to observe the stained cells and the representative fields were captured using the acquisition system cellSense Dimension (Version 4.1). Moreover, the cytomorphologic features and the cell–biomaterial interactions were also highlighted through field-emission scanning electron microscopy (FE-SEM) following a protocol already reported.[50]

Immunocytochemical staining of fibronectin and type I pro-collagen

The fibronectin and type I pro-collagen expression by the CCD-1070Sk cells grown in contact with the analysed substrates was highlighted by means of fluorescent immunocytochemistry staining. Briefly, the human fibroblasts were subjected to a protocol similar to the one described in the above section, where the cells were fixed, permeabilized and blocked, only to be afterwards incubated for 2 h, with anti-fibronectin and anti-pro-collagen type I primary antibodies, respectively (Santa Cruz Biotechnology, dilution 1 : 50). Subsequently, the cells were incubated with an anti-mouse secondary antibody labelled with FITC (Santa Cruz Biotechnology, dilution 1 : 200), in the dark for 1 h. In the end the nuclei were marked with DAPI (4′,6-diamidino-2-phenylindole) and the stained cells were viewed with an inverted fluorescent microscope Olympus IX71 (Olympus, Tokyo, Japan). The representative images were captured with an acquisition system cellSense Dimension (Version 4.1) and the fluorescence intensity was evaluated by calculating the corrected total cell fluorescence (CTCF), in arbitrary units from 12 randomly selected fields for each analysed support, using the ImageJ software (Version 1.52d, National Institute of Health, Bethesda, MD, USA).

Assessment of the macrophage inflammatory activity

In order to observe the inflammatory activity of the RAW 264.7 cells grown in contact with the tested surfaces, the secretion of several inflammatory mediators and the ability to form foreign body giant cells (FBGCs) were assessed. With this in mind, after 2 days of culture, the protein levels of the tumour necrosis factor (TNF)-α, interleukin (IL)-1β and IL-10 released into the medium were quantified using specific sandwich enzyme-linked immunosorbent assay (ELISA) kits, according to the package inserted instructions (R&D Systems, Minneapolis, MN, USA). A microplate reader (FlexStation 3 microplate reader, Molecular Devices, San Jose, CA, USA) was used to determine the optical densities (OD) of the final products and the corresponding concentrations (expressed in pg mL^{-1}) were calculated by reporting to their standard curve. Likewise, the extracellular release of the nitric oxide (NO) was quantified with the help of the Griess reagent (Promega, Madison, WI, USA), as we previously reported.[49] The end product's absorbance was measured with a microplate reader (FlexStation 3 microplate reader, Molecular Devices, USA) and the final nitrite concentration was calculated from a sodium nitrite standard curve.

Moreover, the ability of the PDMS surfaces to determine macrophage to fuse and form FBGCs was investigated after 7 days in culture. The culture medium was changed every 2 days and at day 7 the cells were subjected to the protocol described previously.[49] In the end, the cells labelled with AlexaFluor 488 Phalloidin and DAPI were visualised with an inverted fluorescence microscope (Olympus IX71, Olympus, Tokyo, Japan) and the representative images were captured with the cellSense Dimension acquisition system (Version 4.1). Alongside the qualitative determination, the degree of FBGCs formation was also estimated through a semiquantitative method which involves counting each individual nucleus using the ImageJ operating software. This way the "multinuclear index" could be determined, which represents the percentage of nuclei in multinuclear cells exhibiting at least 3 nuclei against the total number of nuclei from the same microscopic field.

Assessment of the antimicrobial potential

The effects of the obtained PDMS surfaces on three different standard strains (*i.e. S. aureus* (25923 ATCC, Manassas, VA, USA), *E. coli* (25922, ATCC, Manassas, VA, USA) and *C. albicans* (10234, ATCC, Manassas, VA, USA)) were analysed for 2 days, as assumed that biofilm formation can occur within this time frame. The qualitative determination of the antimicrobial potential was performed through the agar diffusion method. In the first stage the microorganisms were grown onto the nutrient agar (PCA-Plate Count Agar) in order to obtain pure standard cultures. In the next step, inoculums with a turbidity adjusted to 0.5 McFarland (corresponding to 10^8 colony-forming units per millilitre (CFU mL^{-1})) were prepared from the pure cultures and 1 mL per sample was aspirated and placed over the 3 types of aliquots: positive control (suspension free of bacteria), smooth and modified PDMS. In the end the samples were incubated overnight, at 37 °C, and the number of forming colonies was counted.

Furthermore, in order to observe the subsequent biofilm evolution on the smooth and modified PDMS surfaces, SEM microscopy was employed, using a similar protocol as described earlier.

Statistical analysis

The obtained data was analysed using the GraphPad Prism software (Version 8, GraphPad, San Diego, CA, USA) *via t*-test/two-way ANOVA with Tukey's multiple comparison tests. All values are expressed as means ± standard deviation (SD) and differences at $p < 0.05$ were considered statistically significant.

Results and discussion

Surface characteristics

Given the implication of chronic inflammation and fibrous encapsulation in the impairment of breast implant functionality and, implicitly its failure, there is a significant interest in exploring new interface designs. Therefore, finding new interface designs by tailoring specific topographical cues in breast implant surfaces that can influence and mitigate FBR, represents a major point of interest. In light of this, new honeycomb like wells microtextured PDMS-based shell interfaces were fabricated through replication on a large-scale using moulds. Compared to salt loss techniques or ADM replica,[40,42] what sets the current design apart is the presence of consistent hexagonal micron-sized units across a large surface area, as opposed to random patterns. This reproducibility offers an improved control and a better understanding of how cells react to specific topographical features, ultimately increasing the ability to predict and improve the implant's outcome.

The SEM and AFM images presented in Fig. 1 reveal the detailed microscale features of the hexagonal matrices. These matrices have specific dimensions, with a lateral size of 51 μm (with a tolerance of ±500 nm), a depth of 5 μm, an internal length of 25 μm per unit, base walls with a width of 17 μm, and ridge tops with a width of 8 μm. Notably, these features were successfully and consistently replicated in PDMS. Moreover, it can be observed that the walls of these matrices are smooth and devoid of debris, displaying a surface roughness measuring below 5 nm, but when considering a larger area, the measured roughness by optical profilometry studies showed values that exceed 12 μm.

When compared to data reported in literature regarding textured surfaces, with values of 8.24 μm for Sa; respectively 40 μm for Sz,[51] the values for the honeycomb surface area were characterized by an increased roughness (Sa = 12.62 μm; Sz = 66.69 μm), especially when compared to that of the smooth replicated surfaces (Sa = 1.74 μm; Sz = 7.14 μm). As seen from the AFM and SEM images (Fig. 1b and c), the replicated PDMS biointerfaces were characterized by a peak-and valley type of profile, containing micro-scale features. Besides Sa parameter, two other height parameters such as skewness (Sku) and kurtosis (Ku) were also considered. Although primarily statistical tools for assessing the central tendency and variability of a dataset, skewness (Sku) and kurtosis offer additional insights into the symmetry and sharpness of surface roughness profiles. Skewness indicates the degree of asymmetry in the roughness distribution, while kurtosis reflects the concentration of surface height deviations around the mean, measuring the sharpness or flatness of the profile. In this study, the textured surface exhibited a positive skewness, indicating an asymmetry with more pronounced peaks than valleys, along with an elevated kurtosis value, suggesting a sharper, more peaked roughness profile (Ssk: 0.735 and Sku: 2.357). In contrast, the smooth silicone implant surfaces were predominantly flat with a positive skewness and excess kurtosis values, thus indicating a rather smooth surface with only some random small nanoscale peaks on the surface (Ssk: 0.027 and Sku: 1.833).

Furthermore, as shown in Fig. 1e, both surfaces were hydrophobic with larger water contact angles of 103° (smooth PDMS surface) and 110° (honeycomb PDMS surface), corresponding to low surface energies of 14 mN m^{-1} and 11 mN m^{-1}, respectively. This hydrophobicity arises from the chemical composition of the polymer: silicone, and its methyl groups ($-CH_3$) together with the presence of low molecular weight molecules on the surface. Since *in vitro* cell culture studies are highly dependent on the ability of cells to adhere, spread, and

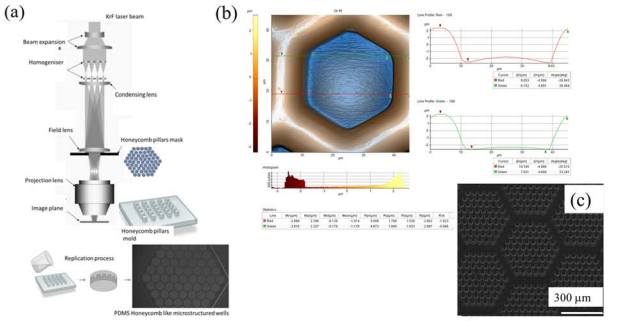

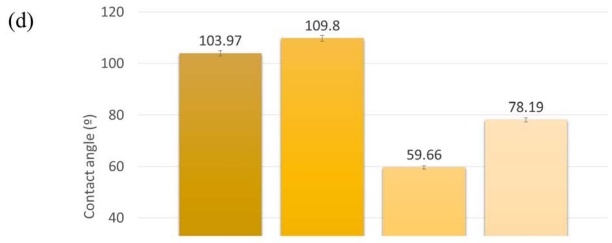

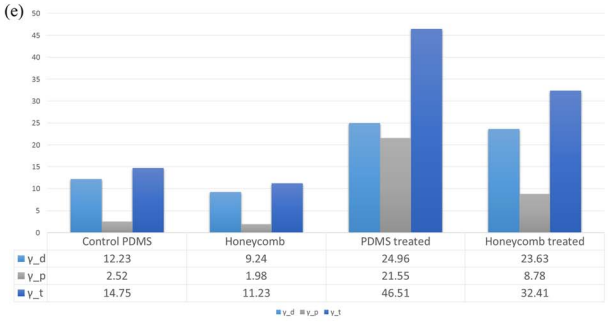

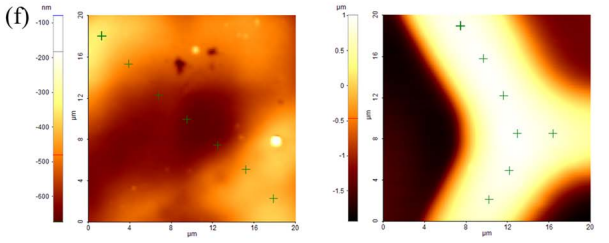

(g)

Spot	F (nN) Flat	F (nN) Structured
1	92	71
2	88	72
3	92	73
4	82	72
5	94	67
6	92	69
7	92	70
Medium value F (nN)	90.29	70.57

Fig. 1 The experimental set-up used to process the moulds and to obtain the replicated textured PDMS (a). Surface characterization by AFM, SEM and wettability measurements: (b) profile of hexagonal unit forming matrices; (c) SEM images of a larger area obtained by PDMS replication. Scale bar 300 µm; (d) contact angle measurements of both treated, structured and untreated surfaces and their corresponding SE (e). The AFM image examples including the distribution of points where adhesion force was measured (f). The values of the adhesion force (in nN) measured on ridges, plateau and flat surfaces (g).

proliferate on the substrate, these types of surfaces tend to repel aqueous solutions and may deter cells from adhering and spreading on said surfaces. With this in mind, UV ozone plasma treatment can be used to control surface alteration with a fundamental change in the wettability through the introduction of polar functional groups onto the hydrophobic substrates. PDMS surfaces exposed to UV ozone were moderately hydrophilic, with water contact angles of 59° and 78°, respectively, and corresponding surface energies of 46 mN m^{-1} and 32 mN m^{-1}, respectively, as shown in Fig. 1e. The observed increase in total surface energy, particularly its polar component, following plasma treatment indicates a significant shift in PDMS surface properties from hydrophobic to hydrophilic. This transformation is attributed to the generation of polar functional groups, such as hydroxyl (–OH) and carboxyl (–COOH), on the surface, enhancing its compatibility with aqueous solutions and biomolecules. This modification facilitates initial passive contact between cell membranes and the biointerface, driven by short-range physicochemical interactions, including van der Waals forces, steric effects, and coulombic forces. While PDMS lacks cell-interacting molecules on its surface, the introduction of functional groups through ozone plasma treatment plays a pivotal role in protein adsorption, providing a foundational platform for integrin binding to cell ligands.[52]

In addition, the AFM adhesion measurements have demonstrated that the detachment force measured on the microstructured areas was approximately 30% greater than on the flat surfaces (90 nN as compared to 70 nN) (Fig. 1f and g), which could be further linked to the way cell–substrate traction force modulates the endogenous tension in the cell–cell and cell–substrate interactions and can impact the optimization substrate design for biomedical applications.[53]

In vitro behaviour of CCD-1070Sk fibroblasts

Fibroblasts' viability and proliferation. Since any modification in the number of cells can be attributed to alterations in their metabolic activity, the CCK-8 assay was performed after 1- and 3-days of culture in order to reveal any differences in the proliferation statuses of the CCD-1070Sk fibroblasts cultured onto the samples' surfaces. The results showed that at both experimental time points, the proliferation rate of the cells seeded onto the honeycomb microtextured PDMS was significantly reduced in comparison to the smooth surface (Fig. 2a). However, a proportional increase in the number of metabolically active viable cells with the incubation period was observed on both substrates, phenomenon which indicates the growth-supporting capacity of the analysed PDMS surfaces.

These findings are also sustained by the results of the live/dead test, which revealed a predominant green fluorescent cellular monolayer (live cells), with major differences in cell density between the two analysed substrates (Fig. 2b). Therefore, the green fluorescent cellular population detected on the smooth surface was higher than that on the honeycomb microtextured substrate, notably after 3 days of culture, showing a decrease in cell density on the microtopographically altered support. Moreover, following a 3 days culture period, on the honeycomb microtextured PDMS, the cells exhibited a tendency to aggregate. This phenomenon is hypothesised to occur as a result of the combined effect of microtopography and

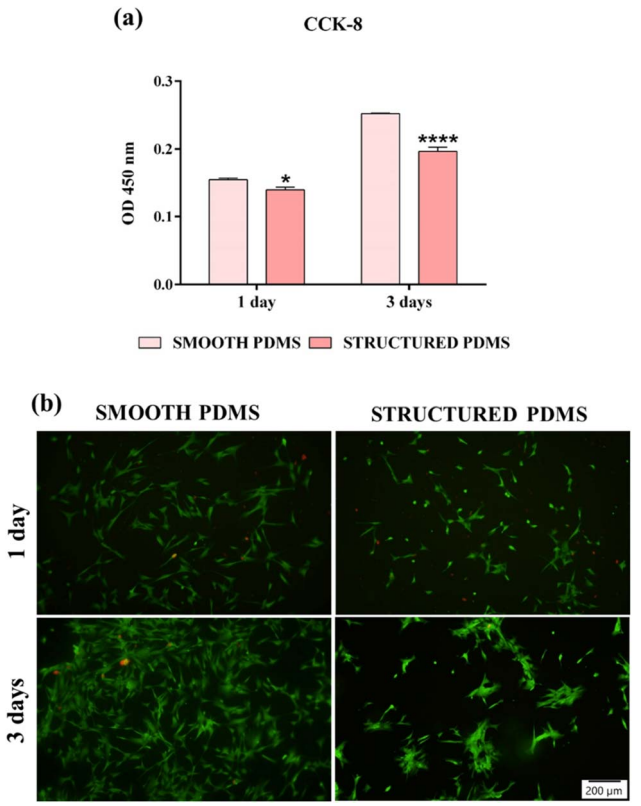

Fig. 2 Viability/proliferation status of the CCD-1070Sk cells grown for 1- and 3-days onto the surface of the honeycomb microtextured and smooth PDMS, as assessed by (a) the CCK-8 test. Results are presented as means ± SD ($n = 3$; ****$p < 0.0001$, *$p < 0.05$ *vs.* smooth PDMS); (b) the live/dead assay (live and dead cells – green and red fluorescence, respectively). Scale bar represents 200 μm.

the hydrophobic recovery of the surface. A review of the literature reveals that attempts to reduce surface hydrophobicity by oxygen/ozone plasma treatment often prove unsuccessful due to the recovery of the surface's hydrophobic nature, which, after a prolonged culture time, led to cell aggregation due to protein dissociation.[54–56] Furthermore, when cultured on a concave grooved surface, a redistribution of cells' adhesion complexes was also observed,[57] which, when combined with the hydrophobic recovery of the surface, may have compelled the cells to form aggregates in order to stay attached to the PDMS.

Fibroblasts' morphological characterization. To observe the impact of the analysed substrates on fibroblasts' morphology, the immunofluorescence staining of the F-actin was performed and the obtained microscopic images highlighted differences in the cytoskeleton organization. As seen in Fig. 3a, the fibroblasts grown onto the surface of the microtextured PDMS displayed a more elongated shape coupled with a reduced area of spreading, while the cells found on the smooth surface exhibited typical morphological characteristics with well-defined actin stress fibres and a larger area of spreading. As established by previous research, the topographical characteristics of a biomaterial's surface have been shown to exert a significant influence on various cellular processes, such as adhesion, spreading and motility.[58–60] On this basis, the observed discrepancies in cell morphology can be attributed to the differences in the characteristics of the analysed surfaces. Thus, the honeycomb microtopography proved to affect the cell–substrate interactions, which can ultimately be translated into alterations in the cytoskeleton structure and its components' distribution. Moreover, these results indicate that the fibroblasts can perceive and interact differently with the altered surface compared to the smooth substrate, therefore displaying a contrasting reorganization of their actin cytoskeleton. Furthermore, it has been demonstrated that smooth PDMS surfaces feature a more uniform cell arrangement, as opposed to the textured silicone-based implants, where fibroblasts are arranged in random patterns based on the surface's morphology variations.[61] This uniform alignment of fibroblasts on the smoother surface has been observed to stimulate the excessive fibroblast growth, which can ultimately result in the development of a capsular contracture[61]

Since the cytoskeleton is a group of dynamic proteins with key roles in cells' adhesion, shape modulation and integrity preservation, vimentin, a type III intermediate filament regarded in literature as a fibroblast marker,[62] was also observed under fluorescence microscopy and the results are presented in Fig. 3a. Similar to the results observed through F-actin labelling, the vimentin expression also revealed a reduced cell density on the honeycomb microtextured PDMS in comparison to the smooth silicone surface, however, with no significant differences in the vimentin intensity fluorescence between the substrates.

In addition, to confirm the fluorescence microscopy observations, SEM microscopy was also employed, and the obtained micrographs revealed that on the microstructured support, the cells were able to adhere over the micropatterned surface but their contact area seemed to be significantly reduced in comparison to the cell-smooth sample contact area (Fig. 3b), as easily can also be noticed in Fig. 3a and b. Taken together, these results indicate that the concave pattern prevented the cells from forming strong contact points with the sample's surface, leading to a reduced cell adhesion and proliferation status, when compared to the smooth PDMS.

Fibronectin and type I pro-collagen production. The desired outcome for any implantable biomedical device is its complete integration into the surrounding tissue, subsequently followed by the full regeneration of the wound. However, in some cases, due to the onset of a prolonged chronic inflammatory response, the fibroblasts migrating to and found at the peri-implant tissue site will produce a highly fibrous, acellular ECM, rich in fibronectin, proteoglycans and type I/III collagens.[63] The sustained and uncontrolled production and deposition of collagen will gradually result in the formation of a thick, avascular fibrous tissue that surrounds the implant and isolates it from the local microenvironment, thus preventing its integration within the tissue and impairing its biocompatibility and efficacy.[64] Since topography can modulate the fibroblasts' activity by altering the cell-surface specific interactions, the influence of the newly developed micropatterned surface on fibronectin network and type I pro-collagen production was investigated at 7 days post-seeding *via* immunofluorescence staining. As shown in

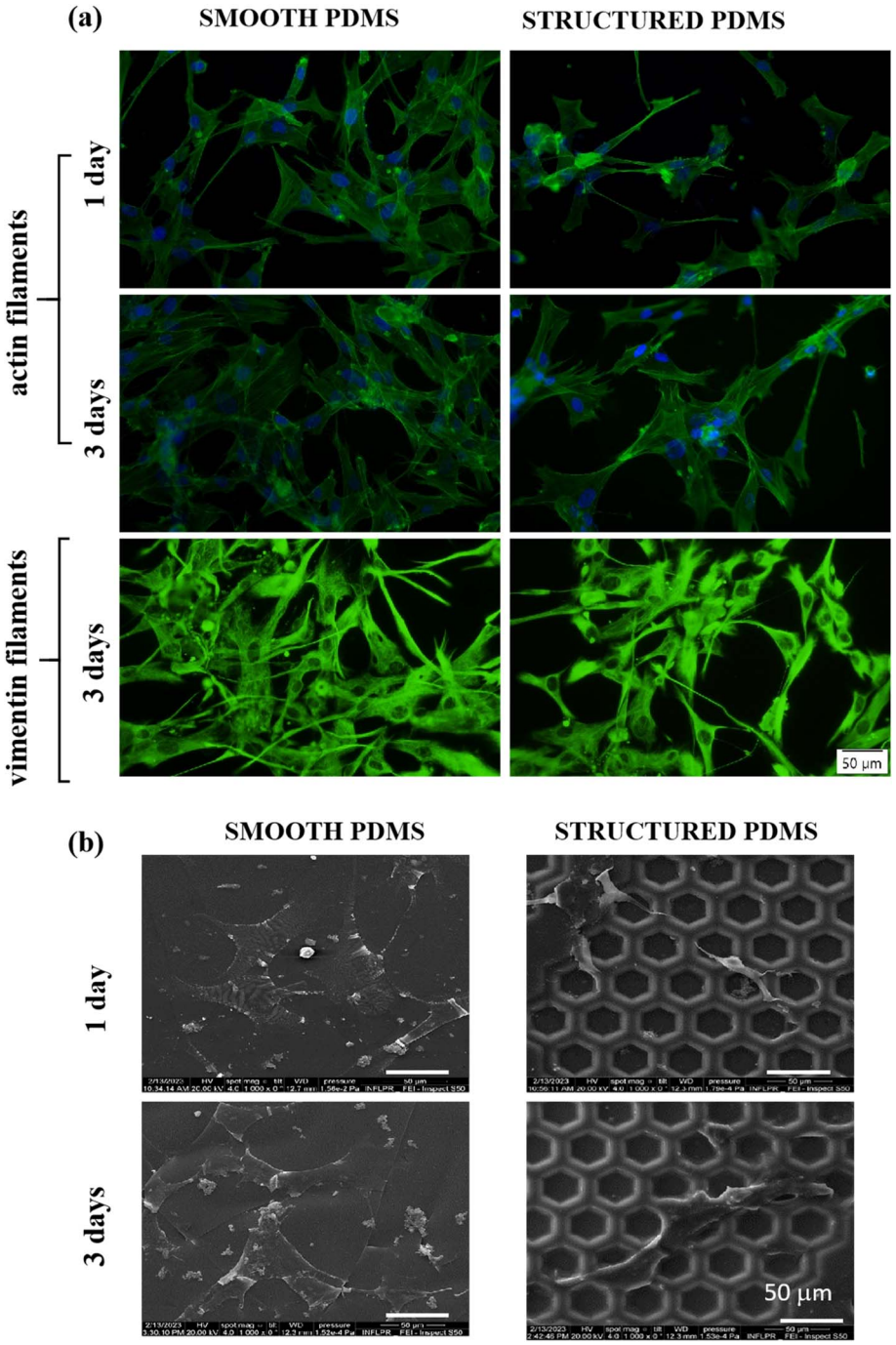

Fig. 3 (a) Fluorescence images of CCD-1070Sk fibroblasts grown for 1- and 3-days in contact with the PDMS surfaces highlighting the actin cytoskeleton (F-actin – green fluorescence), the nuclei (blue fluorescence) and vimentin filaments (green fluorescence). Scale bar represents 50 μm; (b) SEM micrographs of CCD-1070Sk fibroblasts grown onto the surface of the analysed PDMS-based samples after 1- and 3-days of culture. Scale bar represents 50 μm.

Fig. 4a, in the case of the fibroblasts grown onto the microtextured PDMS, the fibronectin signals were less expressed than on the smooth surface, where a higher number of fibronectin fibrils were visible, some of them extending between neighbouring cells (white arrows). In terms of type I pro-collagen production, the immunofluorescent assessment revealed a stronger intracellular staining for the cells found on the smooth PDMS in comparison to the fainter signals observed on the microtextured support. Atlan *et al.* observed that by increasing the intricacy of the surface's topography, the pathophysiology of the FBR was greatly altered, leading to an enhanced tissue ingrowth, responsible for the capsule's disarrangement and increase in tissue adherence.[65]

In addition to the fluorescence microscopy investigations, a quantification of fibronectin and type I pro-collagen fluorescence intensities (Fig. 4b) was also performed and the results

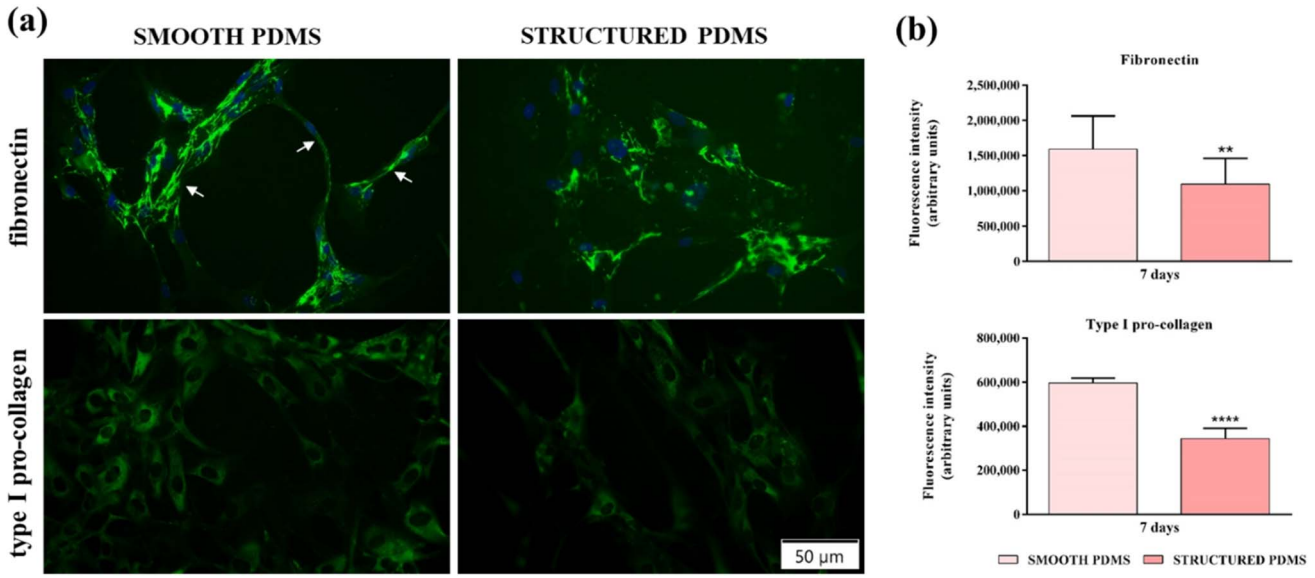

Fig. 4 (a) Immunofluorescent labelling of the fibronectin network and type I pro-collagen synthesized by the CCD-1070SK cells cultured on the analysed surfaces (green fluorescence – positive signals for fibronectin and type I pro-collagen; blue fluorescence – nuclei). The white arrows indicate the better compacted lines of fibronectin fibres developed between adjacent cells on the smooth PDMS surface. Scale bar represents 50 µm; (b) fluorescence intensity measurement ($n = 12$, mean ± SD, ****$p < 0.0001$, **$p < 0.01$ *vs.* smooth PDMS).

corroborate the microscopical observations, indicating that the microtextured surface induced a significant decrease in the aforementioned ECM proteins' expression when compared to the smooth substrate, thus demonstrating their pro-fibrotic suppressing capacity.

Furthermore, fibronectin and type I pro-collagen production may have an indirect implication in bacterial colonisation and biofilm formation. From data reported in the literature, it is clear that many bacterial species produce collagen- and fibronectin-binding proteins that are involved in regulating bacterial attachment to the acellular ECM components[66,67] and that once attached, the bacteria proliferate and form the biofilm. With this in mind, we speculate that a decrease in the collagen and fibronectin network expression may contribute to a reduced bacterial colonisation, biofilm formation and, implicitly, capsular formation.

In vitro immune response of RAW 264.7 monocyte/macrophage-like cells

Macrophages' viability and proliferation. With the knowledge that the immune response can be heavily shaped by the capacity of the biomaterial to sustain the macrophages' survival/proliferation, the viability rate and metabolic activity of the RAW 264.7 cells were investigated, both in the absence and presence of the bacterial agent (100 ng per mL LPS), through the combination of a qualitative assay – live/dead and a quantitative colorimetric CCK-8 test. Fig. 5a reveals a reduction in cell density, but with no visible red-stained dead cells, after LPS treatment, for both surfaces, phenomenon observed more significantly after 3 days of culture compared to the 1 day-time point. However, without LPS stimulation, the number of viable cells grew proportionally with incubation time, on both smooth and microtextured surfaces. In addition, the CCK-8 test was subsequently carried out to corroborate the fluorescence micrographs, and the obtained optical density (OD) values are in agreement with the viability assay results, indicating a statistically significant reduction in the number of viable cells grown in LPS-stimulated conditions after 3 days of culture (Fig. 5b).

Macrophages' morphological features. Since cell spreading and morphology are heavily influenced by the cytoskeleton organization, the actin filament staining with phalloidin conjugated with AlexaFlour 488 was conducted after 1- and 3-days in culture (Fig. 6a). Thus, at the end of the first experimental time point, the macrophages grown in standard culture conditions presented a typical round body with a cortical ring of actin and filopodia extensions around the cell periphery, characteristics specific for unstimulated cells. However, this behaviour was observed more pronounced for the cells grown onto the microtextured PDMS, while the adherent cells found onto the smooth surface exhibited a more elongated, spindle-like shaped cellular body. In contrast, upon LPS treatment, the RAW 264.7 cells exhibited an increase in the cell-support contact area and adopted an altered morphology (*i.e.* elongated or enlarged surfaces with irregular shapes) with multiple filopodia. In literature, these morphological alterations are associated with a migratory, activated, pro-inflammatory phenotype (M1)[68] and were more noticeable after 3 days of culture on both PDMS-based surfaces. In addition, these cells displayed cytoplasmatic-dot like F actin assemblies known as podosomes – micro-sized structures that form at the interface between an adhering cell and the substratum,[69] therefore suggesting an adaptation of macrophage morphology to the substrate contact areas due to the synergetic action of LPS

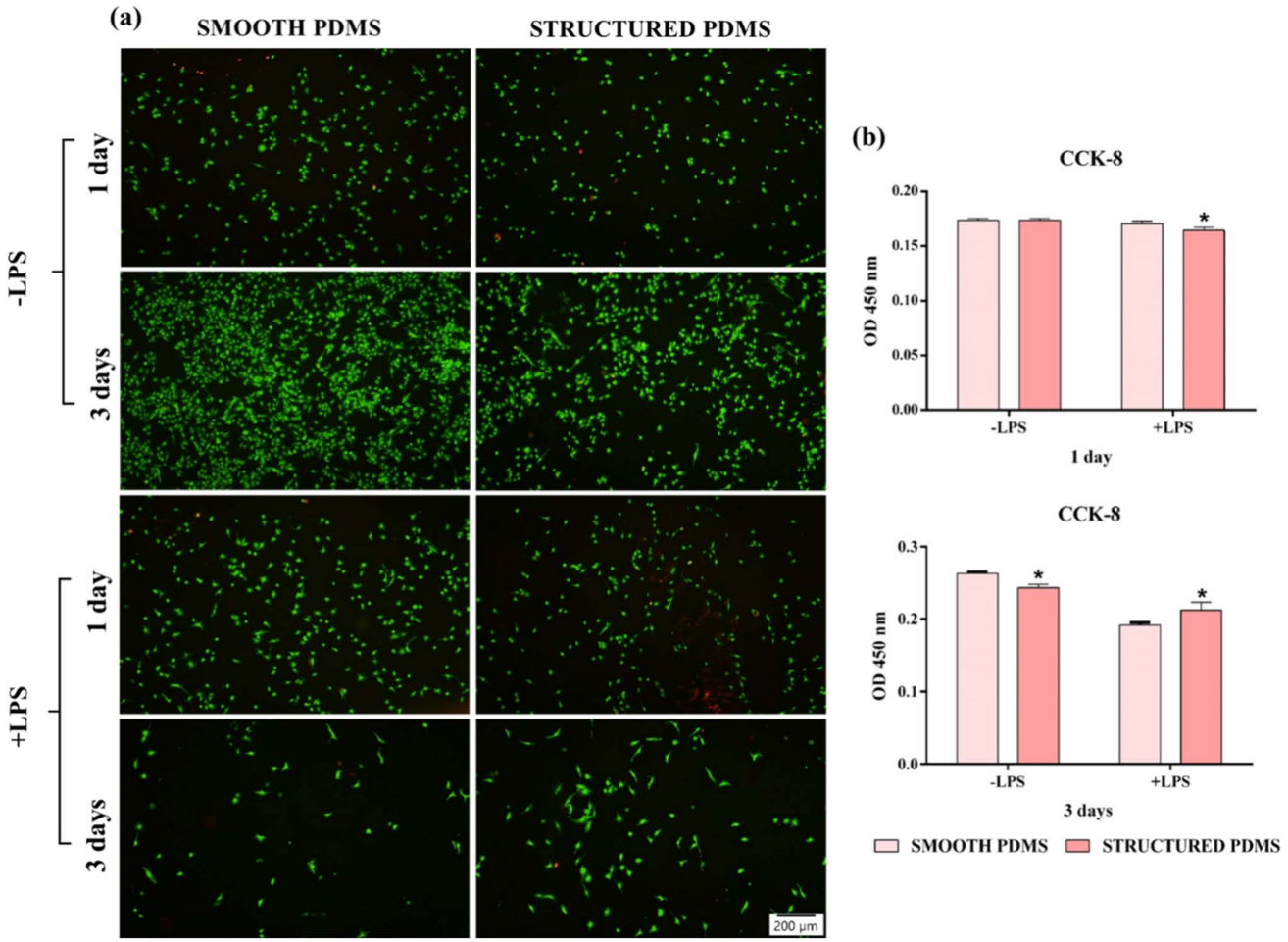

Fig. 5 The viability and proliferation rates of the RAW 264.7 cells cultured directly onto the smooth and honeycomb PDMS surfaces, under standard (−LPS) and LPS-stimulated (+LPS) conditions, after 1- and 3-days of culture. (a) live/dead assay: viable and dead cells – green and red fluorescence, respectively. Scale bar is 200 μm; (b) CCK-8 test. Results are presented as means ± SD ($n = 3$; *$p < 0.05$ *vs.* smooth PDMS).

stimulation and surface microtopography, which can influence the cells' spreading area and the formation of focal adhesion points.[70,71] Furthermore, an increase in cell density with the incubation time could be observed on both surfaces, regardless of LPS treatment. These findings are in line with the reported data regarding the extensive morphological and functional alterations that the activated macrophages exhibit in comparison to the normal, unstimulated cells.[50]

Complementary to the actin cytoskeleton visualisation, SEM micrographs (Fig. 6b) revealed different cell adhesion patterns and morphological characteristics on the microtextured surface as a direct consequence of the cells–microtexture interactions. Previous studies reported on the existence of a curvature-driven behaviour, in which the macrophages tend to actively migrate into regions of negative mean and Gaussian curvatures (*i.e.* concave pits), as long as they exhibit a cell size smaller than the feature size of the curvature landscape.[72] In this light, in our study, the combined preference of macrophages for concave pits and the reduced dimensions of their typical round cellular body, resulted in the complete entrapment of cells within the concave structure, behaviour observed also by Choi *et al.*[73]

Modulation of the macrophages' inflammatory activity. Since each event of the wound healing cascade affects the following one, the early interplay between the implantable biomaterial and the surrounding tissue dictates the status of the activated cells and implicitly the final outcome of the biomaterial and the subsequent phases of the wound healing process. Data reported in literature acknowledge that macrophages involved in the early stage of inflammation play a significant part in the transition process from the acute inflammatory phase to a chronic immune response through the release of certain mediators such as cytokines, chemokines, growth factors, *etc.*[74] Thus, the early cascade of events or plasticity/phenotype of the recruited or already present macrophages is of great importance.[75]

In this context, in order to get an insight into the effects exerted by the PDMS surfaces on the pro- (TNF-α, IL-1β) and anti-inflammatory (IL-10) cytokines' secretion by the LPS-stimulated macrophages, an ELISA assay was performed (Fig. 7a). During the healing process, the pro-inflammatory cytokines have an essential role in the host's adaptive immune system activation,[76] while the anti-inflammatory

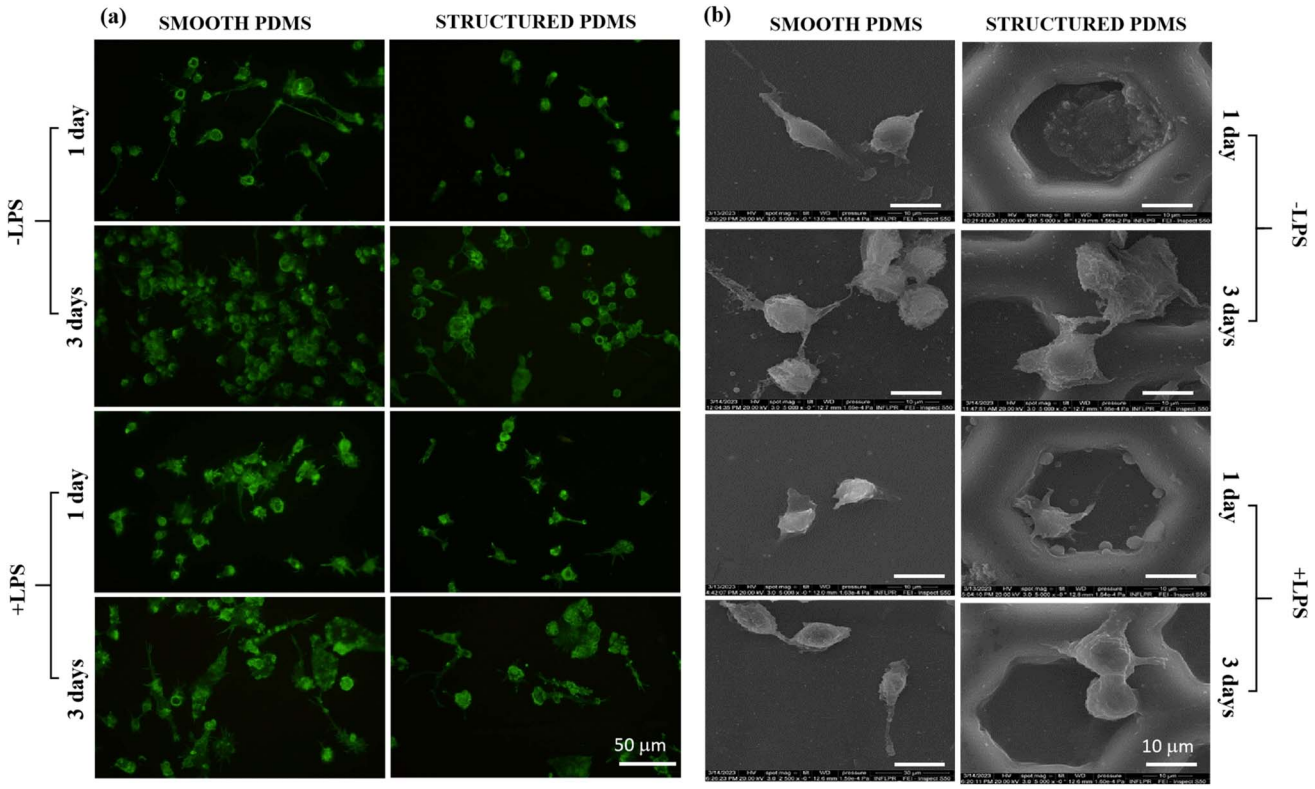

Fig. 6 The morphological characteristics of RAW 264.7 macrophages cultured on the smooth and honeycomb PDMS-based surfaces at 1- and 3-days post-seeding under standard (−LPS) and pro-inflammatory (+LPS) conditions: (a) fluorescence microscopy (actin cytoskeleton – green fluorescence). Scale bar represents 50 μm; (b) SEM microscopy. Scale bar represents 10 μm.

cytokines exhibit protective functions which limit the extent and severity of the inflammatory events.[77] Secreted by the macrophages in the early phase of inflammation, TNF-α is a pro-inflammatory cytokine which regulates the production of other mediators including that of IL-1β and IL-6, and available data indicates that idiosyncrasies in either the secretion or function of TNF-α can play a significant part in various inflammatory impairments.[78] Fig. 7a reveals a down-regulation

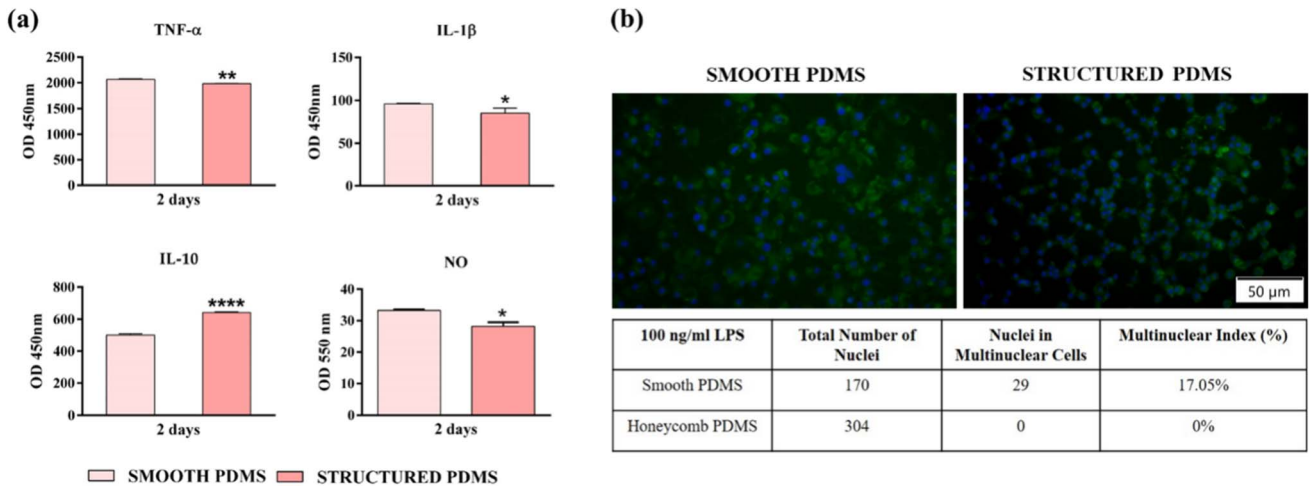

100 ng/ml LPS	Total Number of Nuclei	Nuclei in Multinuclear Cells	Multinuclear Index (%)
Smooth PDMS	170	29	17.05%
Honeycomb PDMS	304	0	0%

Fig. 7 (a) The quantification of the inflammatory mediators secreted from the cells treated with LPS (100 ng mL^{-1}) as assessed by ELISA: TNF-α: $^{**}p < 0.01$ *vs.* smooth PDMS; IL-1β: $^{*}p < 0.05$ *vs.* smooth PDMS; IL-10: $^{****}p < 0.0001$ *vs.* smooth PDMS; NO quantified by Griess diazotization reaction: $^{*}p < 0.05$ *vs.* smooth PDMS. Results are expressed as means ± SD ($n = 3$); (b) fluorescence images showing RAW 264.7 cells' fusion and FBGCs formation on the smooth and honeycomb PDMS surfaces (actin cytoskeleton – green fluorescence; nuclei – blue fluorescence). Scale bar represents 50 μm. The values of the "multinuclear index" as determined by examining 6–10 microscopic fields for each sample.

of the TNF-α protein level secreted in the culture media by macrophages in contact with the microtextured PDMS in comparison to the smooth surface. Similar results were obtained for the pro-inflammatory mediator IL-1β, where a reduction in cytokine secretion was also observed (Fig. 7a). With a biological activity tightly connected to that of TNF-α, IL-1β is a prototypic pro-inflammatory cytokine with a primary role in the activation of the host's immune response towards injury and infection.[79] Another cytokine evaluated in this study was IL-10, a complex, multifunctional anti-inflammatory mediator intimately associated with the fibrotic response through the regulation of the fibro-proliferative process.[80] In contrast to the pro-inflammatory mediators analysed in this study, the IL-10 concentration accumulated in the culture media of macrophages cultured onto the microtextured surface was up-regulated almost to two-folds in comparison to the smooth PDMS (Fig. 7a). In addition, the effect of the PDMS surfaces on the LPS-induced NO production (Fig. 7a) was also investigated and the obtained results revealed that the nitrite level secreted in the culture media by the cells grown onto the structured PDMS was significantly lower when compared to the smooth surface ($p < 0.05$).

Even though various biomaterials can possess an excellent biocompatibility, once introduced in the human body they trigger a host response different from that seen in the normal wound healing process.[81] Whilst the acute inflammatory phases are similar, wound resolution normally ends with tissue regeneration and healing, a stark contrast to implant healing stages, which in most cases is often associated with a chronic inflammatory process. This chronic inflammatory state is known as FBR and is characterized by the recruitment and activation of various immune cells, an intense fibro-proliferative process, and the formation of FBGCs – multinucleated cells involved in material degradation and chronic inflammatory response extension.[82] Data found in literature indicates that the biomaterial-induced FBR could also be influenced and dictated by different surface characteristics including physical features such as topography, shape, size, *etc.*[81] In this light, after 7 days in culture we have evaluated the FBGCs formation (with and without LPS stimulation) with the purpose of determining if the microtextured surface in itself can hinder the macrophage fusion process compared to the smooth PDMS. As shown in Fig. 7b the RAW 264.7 cells grown directly onto the smooth substrate acquired modified morphological features, with larger bodies and numerous nuclei, while on the microtextured surface the cells maintained their typical round shape, with the mention that the cells displayed a topography pattern-guided adhesion, phenomenon not observed at lower cell densities. In addition, the fluorescence microscopy observations are supported by the "multinuclear index" represented in Fig. 7b, which indicates the macrophage fusion suppressing ability of the structured PDMS. Similar results have been reported in literature, indicating that on surfaces with spatially restricted architectures the adherent macrophages exhibited a reduced inflammatory response. For example, in our previous study,[32] PDMS-textured surfaces based on linear step-like features with various multiscaled regular and irregular arrangements and 250 nm step-like types could modulate and supress macrophages' inflammatory activity and bacterial adhesion, respectively. The *in vitro* results demonstrated that by employing an interrupted microline topography on their surface, the PDMS supports were capable to induce a favourable response in terms of cell survival/proliferation, morphological behaviour, and suppression of macrophage fusion into FBGCs, for the regular arrangement of the linear patterns (*i.e.* for Overlapped Linear Pattern—OLP-regular linear step-like feature in an overlapping design with 2 to 3 microns spacing between top structures and a maximum depth of 2 microns; PLP structures—comprising straight, parallel lines, evenly spaced across the surface with line widths of 900 nm up to 1 micrometre, spaced 1 micrometre apart), but also for Overlapped Irregular Linear Patterns-OILP (a combination of overlapped irregular/interrupted 10 to 50 micron-sized length linear patterns) suggesting the importance of using micro-topographies in the process of hindering bacteria adhesion and the macrophage fusion process. While topographies as such have their own advantages, the proposed honeycomb structures address multiple aspects of FBR simultaneously by providing uniform mechanical properties, a controlled cell alignment, a disruption in the fibroblasts' adhesion and a reduction in the macrophages' activation. The geometric control of microstructures at specific scales represents another advantage by the proposed grey level masks assisted laser texturing for moulds production on large areas.

Taken together, the obtained results suggest that the honeycomb microtextured PDMS is capable of inducing the differentiation and polarization of the RAW 264.7 macrophages into the M2 anti-inflammatory phenotype. As evinced by previous studies, anisotropic topographies are capable of modulating the cell responses to different substrata, independently of its various micro- or nano-scale features.[73,83] Furthermore, grooved patterns have been shown to promote the phenotypic differentiation of macrophages towards an M2 anti-inflammatory polarization state,[84] phenomenon also observed in our study. Moreover, it is a well-known fact that macrophages exhibit a natural preference for rougher surfaces, and as reported in literature and corroborated by our results, an increased surface roughness results in a phenotypic switch towards the M2 polarization state.[85]

Antimicrobial activity. Immediately after the introduction of a breast implant, in the host organism, "a race for the surface" arises between the *in situ* cells (platelets, macrophages, fibroblasts) and the competing bacteria to occupy the implant's surface,[86] and even though the surgical procedure is performed under strict aseptic conditions, the occurrence of microbial colonization and biofilm formation on the implant's surface has been frequently documented.[87–89] Biofilms are defined as bacterial communities trapped in a protective matrix, resistant to both the host's immune system and the use of antibiotics.[90] Moreover, they act as a reservoirs for bacterial growth and represent the origin of chronic and/or subclinical infections.[91] Following the capsular contracture, bacterial infections are the subsequent most common complications that frequently demand surgical correction. These infections are thought to

play a significant part in the development of the fibrotic reactions to implants but they are also linked to the occurrence of BIA-ALCL. Topographies with bacteria dimension range were shown to be more effective in suppressing bacteria adherence in a high percentage. For example, biomimetic shark-skin like structures demonstrated that the geometric complexity of the surface has a significant impact on reducing the biofilm formation and swarming motility in *S. aureus* strains, as opposed to the depth of features in grooved patterns.[92] Nevertheless, it was also shown that surface configurations including curvature at the micron scale, appear unfavourable for bacterial attachment despite their larger surface area.[93]

Thus, in order to get an insight into the effects exerted by the PDMS surfaces on the attachment of the three analysed microbial strains, CFU assay as well as SEM imaging was performed after 1 day on both smooth and structured PDMS surfaces. As shown in the SEM images (Fig. 8a), the micro-scale interface PDMS characteristics had a dual impact: hindering *E. coli* and *C. albicans* adhesion but also influencing where the bacteria would attach. As a generally observed trend, on the PDMS smooth control surfaces, especially in the case of *S. aureus*, bacteria were randomly distributed and even formed a biofilm, while on the patterned PDMS films, bacteria tended to occupy the top down rather than the raised patterns preferentially. Moreover, the CFU values decreased less from 10^3 CFU per mL to 10^2 CFU per mL after 1 day for the structured PDMS in the case of *S. aureus*, compared with the smooth support, which kept the number of CFU per mL similar to the suspension control (Fig. 8b). Previously, it was established that the non-specific adhesion of staphylococci relied on hydrophobic interactions and would increase proportionally with the surface's hydrophobicity. However, in this case, the surface's ability to prevent bacterial colonization was linked more to the presence of a micro-topography and less to the wetting characteristics of the PDMS surface. The coverage of *S. aureus* adhering to flat surfaces was notably high. However, the structured PDMS surface remained effective in inhibiting *S. aureus* adhesion when compared to the control surfaces. This finding further stresses the importance of micro-patterned topography in hindering bacterial adhesion, which outweighs the role of surface hydrophobicity.

Moreover, it is generally acknowledged that topographical patterns influence the settlement preferences of various microorganisms, affecting various factors such as adhesion strength, attachment density, and distribution. It has been hypothesized that microorganisms tend to maximize the area of contact with a surface or to bind preferentially to specific areas that provide a high number of attachment points. Recently, these selective mechanisms have been associated with a trade-off in the cellular adhesion process, as surface configurations featuring local curvature at the micron and submicron scale (*e.g.* hemispherical patterns) appear unfavourable for bacterial attachment despite their larger surface area.[93]

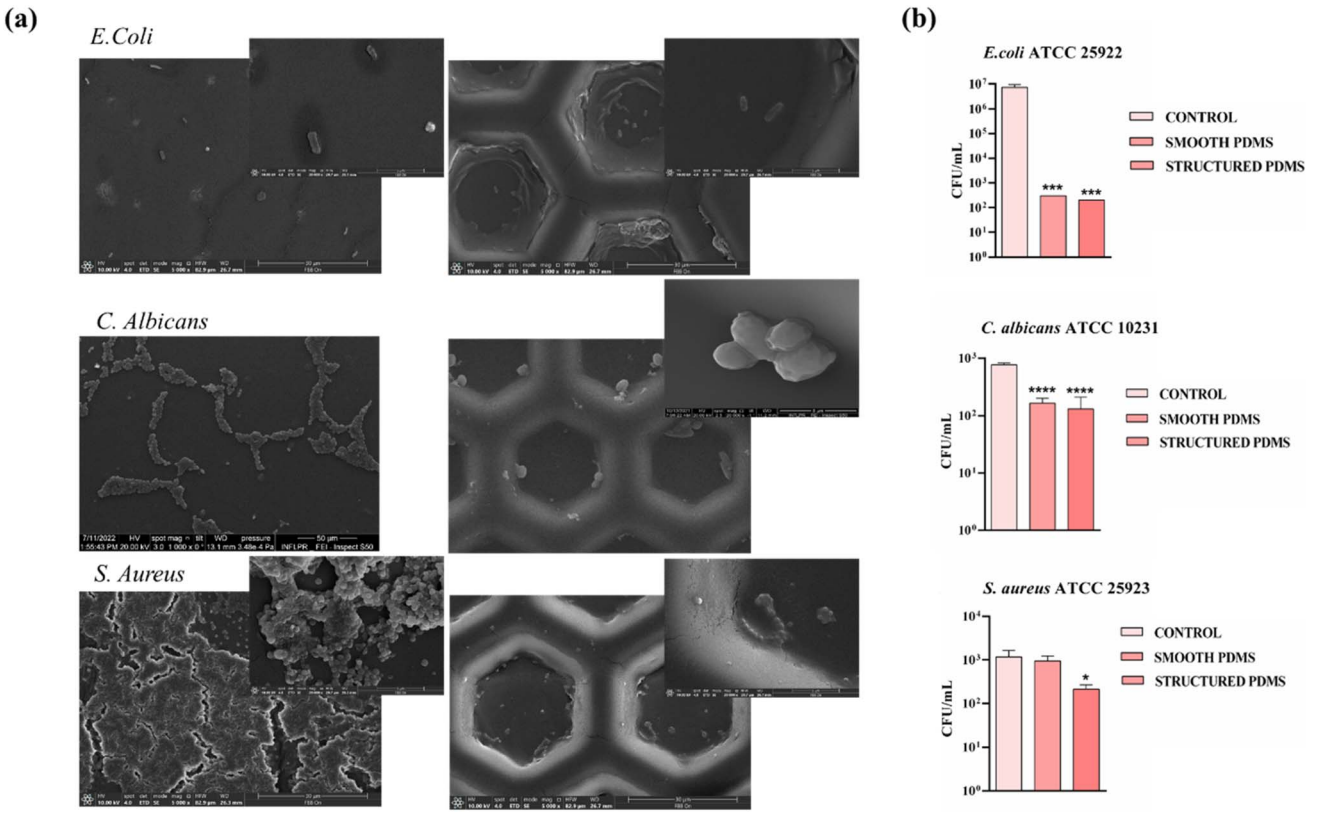

Fig. 8 (a) SEM micrographs after 1 day of incubation with microbial suspensions on the honeycomb PDMS support; (b) colony forming unit (CFU) analysis of *S. aureus*; *E. coli* and *C. albicans* after 1 day. Results are presented as means ± SD ($n = 3$) (****$p < 0.0001$, ***$p < 0.001$, *$p < 0.05$ *vs.* control).

Conclusions

Novel honeycomb-patterned wells microtextured PDMS surfaces were successfully obtained through an innovative 3D grayscale fabrication process combined with replication addressing the challenges associated with chronic inflammation and fibrous encapsulation of breast implants. The unique aspect of this design is the presence of consistent hexagonal micron-sized units across a large surface area, providing improved control and scalable process for obtaining large area for understanding of how cells react to specific topographical features.

The *in vitro* biological investigations demonstrated that the newly designed microtextured surface was cytocompatible and capable of limiting the formation of the fibrotic capsule by inducing an attenuated immune response, which should discourage the production and deposition of fibrous tissue at the biomaterial-breast tissue interface, therefore reducing the capsular contracture phenomenon.

Taking into consideration the aforementioned results, we can postulate that the biological behaviour of various cells, in this case fibroblasts and macrophages, on silicone surface patterns can be customized in order to obtain the desired physiological changes in the cells targeting the development of new biointerfaces with controlled features able of mitigating capsular contracture through the manipulation of the FBR. However, despite the promising *in vitro* results, further studies are necessary to fully characterise the effect of microtexturing on capsule formation inhibition. For example, the immune response elicited by a biomaterial is an intricate process involving a complex interplay between a series of factors, in which their effective regulation is paramount for the successful implantation of the biomaterial. Furthermore, the breast capsule is composed of myofibroblasts, which are cells of significant importance in the pathophysiology of breast implant contracture, reason why they should also be investigated. Last but not least, the short-term *in vitro* assessment should be followed by a long-term *in vivo* study in which the effects of the microtextured honeycomb PDMS are investigated with the use of an appropriate animal model.

Data availability

The datasets supporting this article have been included in the manuscript and any other ESI data† (*e.g.* different magnification for SEM images, tables) can be provided by the authors of the manuscript on request.

Author contributions

Andreea Mariana Negrescu: conceptualization, methodology: *in vitro* experiments, validation, writing – original draft. Simona Nistorescu: methodology: *in vitro* experiments, validation, writing – original draft. Anca Bonciu: methodology: SEM, CA and SE analysis, validation, writing – original draft. Laurentiu Rusen: methodology, writing – original draft. Nicoleta Dumitrescu: methodology, writing – original draft. Iuliana Urzica: methodology: profilometry. Antoniu Moldovan: methodology, AFM measurements, Gratiela Gradisteanu: methodology: microbiology experiments, Patrick Hoffmann: methodology: assistance and acces to grey level mask laser assisted system for mold production on large area. Anisoara Cimpean: conceptualization, supervision, writing & editing. Valentina Dinca: conceptualization, funding acquisition, supervision, validation, writing & editing. The manuscript was written through contributions of all authors. All authors have given approval to the final version of the manuscript.

Conflicts of interest

There are no conflicts to declare.

Acknowledgements

This work was supported by grants from the Romanian Ministry of Education and Research, CCCDI-UEFISCDI, project number PN-III-P4-ID-PCE-2020-2375 and project number PN-IV-P2-2.1-TE-2023-1347. Authors acknowledge Erdem C. Siringil and Karl L. Boehlen for their advice, support and thoughtful insights during the mould production at Laboratory for Advanced Materials Processing, EMPA.

References

1 F. S. di Pompeo, G. Paolini, G. Firmani and M. Sorotos, *JPRAS Open*, 2022, **32**, 166–177.
2 A. H. Chao, R. Garza and S. P. Povoski, *Expert Rev. Med. Devices*, 2016, **13**, 143–156.
3 Plastic Surgery Statistics, American Society of Plastic Surgeons, **https://www.plasticsurgery.org/news/plastic-surgery-statistics**, accessed 13 October 2023.
4 S. Łukasiewicz, M. Czeczelewski, A. Forma, J. Baj, R. Sitarz and A. Stanisławek, *Cancers*, 2021, **13**, 4287.
5 C. R. Albornoz, P. B. Bach, B. J. Mehrara, J. J. Disa, A. L. Pusic, C. M. McCarthy, P. G. Cordeiro and E. Matros, *Plast. Reconstr. Surg.*, 2013, **131**, 15–23.
6 I. Fanakidou, S. Zyga, V. Alikari, M. Tsironi, J. Stathoulis and P. Theofilou, *Qual. Life Res.*, 2018, **27**, 539–543.
7 L. Fortunato, A. Loreti, G. Cortese, D. Spallone, V. Toto, F. Cavaliere, M. Farina, M. La Pinta, E. Manna, L. Detto and T. Pallara, *Clin. Breast Cancer*, 2021, **21**, 162–169.
8 R. M. Miseré, S. M. van Kuijk, E. L. Claassens, E. M. Heuts, A. A. Piatkowski and R. R. van der Hulst, *Breast*, 2021, **59**, 176–182.
9 V. Lemaine, S. R. Schilz, H. K. Van Houten, L. Zhu, E. B. Habermann and J. C. Boughey, *Plast. Reconstr. Surg.*, 2020, **145**, 303–311.
10 R. B. Taylor, D. E. Eldred, G. Kim, J. M. Curtis, H. J. Brandon and P. C. Klykken, *J. Biomed. Mater. Res., Part A*, 2008, **85**, 684–691.
11 B. P. Bengtson and F. F. Eaves, *Aesthetic Surg. J.*, 2012, **32**, 157–174.
12 N. M. Cole, *Plast. Reconstr. Surg.*, 2018, **141**, 1137–1141.

13 B. E. Cohen, T. M. Biggs, E. D. Cronin and D. R. Collins, *Plast. Reconstr. Surg.*, 1997, **99**, 1597–1601.
14 S. L. Brown, G. Pennello, W. A. Berg, M. S. Soo and M. S. Middleton, *J. Rheumatol.*, 2001, **28**(5), 996–1003.
15 T. F. Henriksen, J. P. Fryzek, L. R. Hölmich, J. K. McLaughlin, K. Kjøller, A. P. Høyer, J. H. Olsen and S. Friis, *Ann. Plast. Surg.*, 2005, **54**, 343–351.
16 G. S. Brody, *Plast. Reconstr. Surg.*, 1997, **100**, 1314–1321.
17 J. C. McDonald and G. M. Whitesides, *Acc. Chem. Res.*, 2002, **35**, 491–499.
18 A. Araco, R. Caruso, F. Araco, J. Overton and G. Gravante, *Plast. Reconstr. Surg.*, 2009, **124**, 1808–1819.
19 J. E. Puskas, E. A. Foreman-Orlowski, G. T. Lim, S. E. Porosky, M. M. Evancho-Chapman, S. P. Schmidt, M. El Fray, M. Piatek, P. Prowans and K. Lovejoy, *Biomaterials*, 2010, **31**, 2477–2488.
20 S. H. Kang, C. Sutthiwanjampa, C. Y. Heo, W. S. Kim, S. H. Lee and H. Park, *Int. J. Mol. Sci.*, 2018, **19**(4), 1171.
21 A. Araco, G. Gravante, F. Araco, D. Delogu and V. Cervelli, *Plast. Reconstr. Surg.*, 2006, **118**, 1499–1500.
22 O. Veiseh and A. J. Vegas, *Adv. Drug Delivery Rev.*, 2019, **144**, 148–161.
23 W. J. Pangsaan and A. W. Comstock, *US Pat.*, US3559214A, 1965, vol. 461, p. 326.
24 N. Castel, T. Soon-Sutton, P. Deptula, A. Flaherty and F. Don Parsa, *Arch. Plast. Surg.*, 2015, **42**, 186.
25 B. Y. Yoo, B. H. Kim, J. S. Lee, B. H. Shin, H. Kwon, W. G. Koh and C. Y. Heo, *Acta Biomater.*, 2018, **76**, 56–70.
26 I. Brigaud, C. Garabédian, N. Bricout, L. Pieuchot, A. Ponche, R. Deltombe, R. Delille, M. Atlan, M. Bigerelle and K. Anselme, *Plast. Reconstr. Surg.*, 2020, **145**, 542E–551E.
27 A. M. Danino, P. Basmacioglu, S. Saito, F. Rocher, C. Blanchet-Bardon, M. Revol and J. M. Servant, *Plast. Reconstr. Surg.*, 2001, **108**, 2047–2052.
28 F. Jalalabadi, A. F. Doval, V. Neese, E. Andrews and A. J. Spiegel, *Plast. Reconstr. Surg. Glob. Open*, 2021, **9**, E3449.
29 H. Hu, K. Johani, A. Almatroudi, K. Vickery, B. Van Natta, M. E. Kadin, G. Brody, M. Clemens, C. Y. Cheah, S. Lade, P. A. Joshi, H. M. Prince and A. K. Deva, *Plast. Reconstr. Surg.*, 2016, **137**, 1659–1669.
30 M. E. Kadin, A. Deva, H. Xu, J. Morgan, P. Khare, R. A. F. MacLeod, B. W. Van Natta, W. P. Adams, G. S. Brody and A. L. Epstein, *Aesthetic Surg. J.*, 2016, **36**, 773–781.
31 I. Schoberleitner, K. Faserl, C. H. Tripp, E. J. Pechriggl, S. Sigl, A. Brunner, B. Zelger, N. Hermann-Kleiter, L. Baier, T. Steinkellner, B. Sarg, D. Egle, C. Brunner and D. Wolfram, *Front. Immunol.*, 2024, **15**, 1342895.
32 A. M. Negrescu, S. Nistorescu, A. F. Bonciu, L. Rusen, L. N. Dumitrescu, I. Urzica, A. Cimpean and V. Dinca, *Polymers*, 2024, **16**, 3046.
33 L. E. Sima, A. Bonciu, M. Baciu, I. Anghel, L. N. Dumitrescu, L. Rusen and V. Dinca, *Nanomaterials*, 2020, **10**, 1–25.
34 M. Asadi Tokmedash, C. Kim, A. P. Chavda, A. Li, J. Robins and J. Min, *Biomaterials*, 2025, **319**, 123136.
35 K. Yang, J. Shi, L. Wang, Y. Chen, C. Liang, L. Yang and L. N. Wang, *J. Mater. Sci. Technol.*, 2022, **99**, 82.
36 S. Zheng, M. Bawazir, A. Dhall, H. E. Kim, L. He, J. Heo and G. Hwang, *Front. Bioeng. Biotechnol.*, 2021, **9**, 643722.
37 D. P. Linklater, V. A. Baulin, S. Juodkazis, R. J. Crawford, P. Stoodley and E. P. Ivanova, *Nat. Rev. Microbiol.*, 2020, **19**(1), 8–22.
38 F. Robotti, S. Bottan, F. Fraschetti, A. Mallone, G. Pellegrini, N. Lindenblatt, C. Starck, V. Falk, D. Poulikakos and A. Ferrari, *Sci. Rep.*, 2018, **8**(1), 1–13.
39 S. Chen, J. A. Jones, Y. Xu, H. Y. Low, J. M. Anderson and K. W. Leong, *Biomaterials*, 2010, **31**, 3479–3491.
40 J. C. Doloff, O. Veiseh, R. de Mezerville, M. Sforza, T. A. Perry, J. Haupt, M. Jamiel, C. Chambers, A. Nash, S. Aghlara-Fotovat, J. L. Stelzel, S. J. Bauer, S. Y. Neshat, J. Hancock, N. A. Romero, Y. E. Hidalgo, I. M. Leiva, A. M. Munhoz, A. Bayat, B. M. Kinney, H. C. Hodges, R. N. Miranda, M. W. Clemens and R. Langer, *Nat. Biomed. Eng.*, 2021, **5**, 1115–1130.
41 Y. Xu, K. S. Phillips and D. Ren, *Acta Biomater.*, 2024, **187**, 253–260.
42 D. J. T. Kyle, A. Oikonomou, E. Hill and A. Bayat, *Biomaterials*, 2015, **52**, 88–102.
43 F. T. Foroushani, K. Dzobo, N. P. Khumalo, V. Z. Mora, R. de Mezerville and A. Bayat, *Biomater. Res.*, 2022, **26**, 1–27.
44 P. K. Chaudhuri, C. Q. Pan, B. C. Low and C. T. Lim, *Sci. Rep.*, 2016, **6**, 19672.
45 A. M. Schmidt, S. R. Fagerer, K. Jefimovs, F. Buettner, C. Marro, E. C. Siringil, K. L. Boehlen, M. Pabst and A. J. Ibáñez, *Analyst*, 2014, **139**, 5709–5717.
46 D. K. Owens and R. C. Wendt, *J. Appl. Polym. Sci.*, 1969, **13**, 1741–1747.
47 P. Neacsu, A. Mazare, A. Cimpean, J. Park, M. Costache, P. Schmuki and I. Demetrescu, *Int. J. Biochem. Cell Biol.*, 2014, **55**, 187–195.
48 A. M. Negrescu, V. Mitran, W. Draghicescu, S. Popescu, C. Pirvu, I. Ionascu, T. Soare, S. Uzun, S. M. Croitoru and A. Cimpean, *J. Funct. Biomater.*, 2022, **13**, 43.
49 A. M. Negrescu, M. G. Necula, A. Gebaur, F. Golgovici, C. Nica, F. Curti, H. Iovu, M. Costache and A. Cimpean, *Int. J. Mol. Sci.*, 2021, **22**, 1–36.
50 M. G. Necula, A. Mazare, A. M. Negrescu, V. Mitran, S. Ozkan, R. Trusca, J. Park, P. Schmuki and A. Cimpean, *Int. J. Mol. Sci.*, 2022, **23**, 3558.
51 A. M. Munhoz, M. W. Clemens and M. Y. Nahabedian, *Plast. Reconstr. Surg. Glob. Open*, 2019, **7**, E2466.
52 F. Viela, D. Granados, A. Ayuso-Sacido and I. Rodríguez, *Adv. Funct. Mater.*, 2016, **26**, 5599–5609.
53 V. Maruthamuthu, B. Sabass, U. S. Schwarz and M. L. Gardel, *Proc. Natl. Acad. Sci. U. S. A.*, 2011, **108**, 4708–4713.
54 Y. J. Chuah, Y. T. Koh, K. Lim, N. V. Menon, Y. Wu and Y. Kang, *Sci. Rep.*, 2016, **5**, 18162.
55 Y. J. Chuah, S. Kuddannaya, M. H. A. Lee, Y. Zhang and Y. Kang, *Biomater. Sci.*, 2015, **3**, 383–390.
56 S. Kuddannaya, Y. J. Chuah, M. H. A. Lee, N. V. Menon, Y. Kang and Y. Zhang, *ACS Appl. Mater. Interfaces*, 2013, **5**, 9777–9784.
57 L. G. Zhang, D. H. Zhong, Y. Zhang, C. Z. Li, W. S. Kisaalita and Z. Z. Wu, *Biomaterials*, 2014, **35**, 9423–9437.

58 J. Luo, M. Walker, Y. Xiao, H. Donnelly, M. J. Dalby and M. Salmeron-Sanchez, *Bioact. Mater.*, 2022, **15**, 145–159.
59 B. K. K. Teo, S. T. Wong, C. K. Lim, T. Y. S. Kung, C. H. Yap, Y. Ramagopal, L. H. Romer and E. K. F. Yim, *ACS Nano*, 2013, **7**, 4785–4798.
60 M. J. Dalby, M. O. Riehle, D. S. Sutherlad, H. Agheli and A. S. G. Curtis, *Eur. J. Cell Biol.*, 2004, **83**, 159–169.
61 H. J. Jeon, M. J. Kang, J. S. Lee, J. Kang, E. A. Kim, H. K. Jin, J. sung Bae and J. D. Yang, *Sci. Rep.*, 2022, **12**, 13535.
62 N. Wang and D. Stamenovic, *J. Muscle Res. Cell Motil.*, 2002, **23**, 535–540.
63 D. Akilbekova and K. M. Bratlie, *PLoS One*, 2015, **10**(6), e0130386.
64 A. Kim, M. A. Downer, C. E. Berry, C. Valencia, A. Z. Fazilat and M. Griffin, *Bioengineering*, 2023, **10**, 1411.
65 M. Atlan, G. Nuti, H. Wang, S. Decker and T. A. Perry, *J. Mech. Behav. Biomed. Mater.*, 2018, **88**, 377–385.
66 D. J. Vaca, A. Thibau, M. Schütz, P. Kraiczy, L. Happonen, J. Malmström and V. A. J. Kempf, *Med. Microbiol. Immunol.*, 2020, **209**, 277–299.
67 M. Bhattacharya and A. R. Horswill, *FEMS Microbiol. Rev.*, 2024, **48**(1), fuae002.
68 F. Y. McWhorter, T. Wang, P. Nguyen, T. Chung and W. F. Liu, *Proc. Natl. Acad. Sci. U. S. A.*, 2013, **110**, 17253–17258.
69 E. Van Goethem, R. Guiet, S. Balor, G. M. Charrière, R. Poincloux, A. Labrousse, I. Maridonneau-Parini and V. Le Cabec, *Eur. J. Cell Biol.*, 2011, **90**, 224–236.
70 F. Y. McWhorter, C. T. Davis and W. F. Liu, *Cell. Mol. Life Sci.*, 2015, **72**, 1303–1316.
71 H. S. Lee, S. J. Stachelek, N. Tomczyk, M. J. Finley, R. J. Composto and D. M. Eckmann, *J. Biomed. Mater. Res., Part A*, 2013, **101**, 203.
72 S. J. P. Callens, R. J. C. Uyttendaele, L. E. Fratila-Apachitei and A. A. Zadpoor, *Biomaterials*, 2020, **232**, 119739.
73 J. Choi, B. H. Shin, T. Kim, J. S. Lee, S. Kim, Y. Bin Choy, C. Y. Heo and W. G. Koh, *Mater. Sci. Eng., C*, 2022, **135**, 112687.
74 T. J. Koh and L. A. DiPietro, *Expert Rev. Mol. Med.*, 2011, **13**, e23.
75 J. M. Anderson, A. Rodriguez and D. T. Chang, *Semin. Immunol.*, 2008, **20**, 86–100.
76 C. Schlundt, T. El Khassawna, A. Serra, A. Dienelt, S. Wendler, H. Schell, N. van Rooijen, A. Radbruch, R. Lucius, S. Hartmann, G. N. Duda and K. Schmidt-Bleek, *Bone*, 2018, **106**, 78–89.
77 J. A. Oliveira, R. de Oliveira Alves, I. M. Nascimento, M. A. R. Hidalgo, R. M. Scarel-Caminaga and S. Cristina Pigossi, *BMC Oral Health*, 2023, **23**, 420.
78 M. Qiang and K. Kinneer, *J. Biol. Chem.*, 2002, **277**, 2477–2484.
79 J. M. Cavaillon, *Cell. Mol. Biol.*, 2001, **47**, 695–702.
80 E. H. Steen, X. Wang, S. Balaji, M. J. Butte, P. L. Bollyky and S. G. Keswani, *Adv. Wound Care*, 2020, **9**, 184.
81 S. Franz, S. Rammelt, D. Scharnweber and J. C. Simon, *Biomaterials*, 2011, **32**, 6692–6709.
82 Z. Sheikh, P. J. Brooks, O. Barzilay, N. Fine and M. Glogauer, *Materials*, 2015, **8**, 5671–5701.
83 Y. L. Jung and H. J. Donahue, *Tissue Eng.*, 2007, **13**, 1879–1891.
84 T. U. Luu, S. C. Gott, B. W. K. Woo, M. P. Rao and W. F. Liu, *ACS Appl. Mater. Interfaces*, 2015, **7**, 28665–28672.
85 K. A. Barth, J. D. Waterfield and D. M. Brunette, *J. Biomed. Mater. Res., Part A*, 2013, **101**, 2679–2688.
86 I. Schoberleitner, K. Faserl, M. Lackner, D. C. Coraça-Huber, A. Augustin, A. Imsirovic, S. Sigl and D. Wolfram, *Biomolecules*, 2024, **14**, 1433.
87 U. M. Rieger, J. Mesina, D. F. Kalbermatten, M. Haug, H. P. Frey, R. Pico, R. Frei, G. Pierer, N. J. Lüscher and A. Trampuz, *Br. J. Surg.*, 2013, **100**, 768–774.
88 S. J. Chong and A. K. Deva, *Clin. Plast. Surg.*, 2015, **42**, 427–436.
89 F. Carmona-Torre, L. Fernández-Ciriza, C. Berniz, C. Gomez-Martinez de Lecea, A. Ramos, B. Hontanilla and J. L. del Pozo, *Microorganisms*, 2022, **10**, 2004.
90 S. Bano, N. Hassan, M. Rafiq, F. Hassan, M. Rehman, N. Iqbal, H. Ali, F. Hasan and Y. Q. Kang, *Microorganisms*, 2023, **11**, 2595.
91 L. K. Vestby, T. Grønseth, R. Simm and L. L. Nesse, *Antibiotics*, 2020, **9**, 59.
92 A. Sakamoto, Y. Terui, C. Horie, T. Fukui, T. Masuzawa, S. Sugawara, K. Shigeta, T. Shigeta, K. Igarashi and K. Kashiwagi, *FEMS Microbiol. Lett.*, 2014, **361**, 10–16.
93 Y. R. Chang, E. R. Weeks and W. A. Ducker, *ACS Appl. Mater. Interfaces*, 2018, **10**, 9225–9234.